ACS OMEGA

http://pubs.acs.org/journal/acsodf

Article

Molecular Dynamics Simulations of Nitrate/MgO Interfaces and Understanding Metastability of Thermochemical Materials

Alexandr Shkatulov,* Bahanur Becit, and Dirk Zahn

Cite This: *ACS Omega* 2022, 7, 16371−16379

Read Online

ACCESS | Metrics & More | Article Recommendations | Supporting Information

ABSTRACT: We explore the role of molten nitrate interfaces on MgO surface treatment for improving the reversibility of thermochemical energy storage via sorption and desorption of water or CO_2. Our molecular dynamics simulations focus on melts of $LiNO_3$, $NaNO_3$, KNO_3, and the triple eutectic mixture $Li_{0.38}Na_{0.18}K_{0.44}NO_3$ on the surface of MgO to provide atomic scale details of adsorbed layers and to rationalize interface energies. On this basis, a thermodynamic model is elaborated to characterize the effect of nitrate melts on the dehydration of $Mg(OH)_2$ and to quantitatively explain the difference in dehydration temperatures of intact and $LiNO_3$-doped $Mg(OH)_2$.

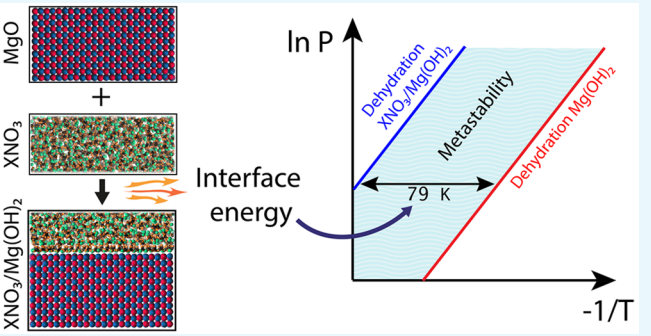

INTRODUCTION

Efficient and sustainable energy systems are unimaginable without means of reliable and inexpensive energy storage.[1] Harnessing solar power[2] or utilization of industrial waste heat on a large scale[3−5] calls for scalable thermal energy storage at 200−600 °C to harmonize energy production and consumption in space and time.

Currently, the use of reversible chemical reactions for thermal energy storage—also known as thermochemical energy storage (TCES)—is attracting attention due to potentially high heat storage density and versatility of chemical heat batteries.[6−8] Advent of this technology in the past decade incites fundamental research on materials reactivity with the goal to enhance the kinetic performance.[9]

One of the promising materials for TCES is MgO which can reversibly absorb water yielding magnesium hydroxide:

$$MgO + H_2O = Mg(OH)_2 \qquad \Delta_r H^\circ = 81.6\ kJ/mol \tag{1}$$

The MgO-based thermal batteries are charged by dehydration of $Mg(OH)_2$ consuming heat (Figure 1). During this process, the material transforms to MgO while releasing H_2O. The consumed heat is hence stored in the form of the lattice energy of MgO. When needed, the system may be discharged in a controlled manner triggering heat release by the addition of water vapor, hence hydrating back to the "discharged" state. A similar cycle can be realized with CO_2 instead of H_2O and $MgCO_3$ instead of $Mg(OH)_2$, respectively, by the help of sophisticated catalysts.[10]

One of the challenges hindering the industrial application of this scheme is the low reactivity in both charging and release processes. This leads to extended metastability zones such that

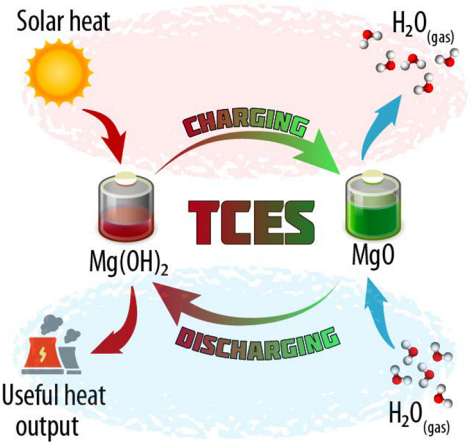

Figure 1. Operation principle of a thermochemical heat battery based on the transformation of $Mg(OH)_2$ to MgO for energy storage (charging) and its reverse reaction for energy release (discharging), respectively. Charging driven by solar heat (upper left arrow) is accompanied by the decomposition of $Mg(OH)_2$ with simultaneous release of water (upper right arrow). Discharging driven by absorption of water (lower right arrow) is accompanied by emission of useful heat (lower left arrow).

Received: January 6, 2022
Accepted: April 14, 2022
Published: May 2, 2022

https://doi.org/10.1021/acsomega.2c00095
ACS Omega 2022, 7, 16371−16379

in order to decompose $Mg(OH)_2$ or $MgCO_3$ one has to overheat[17] or undercool[11] considerably (Figure 2).

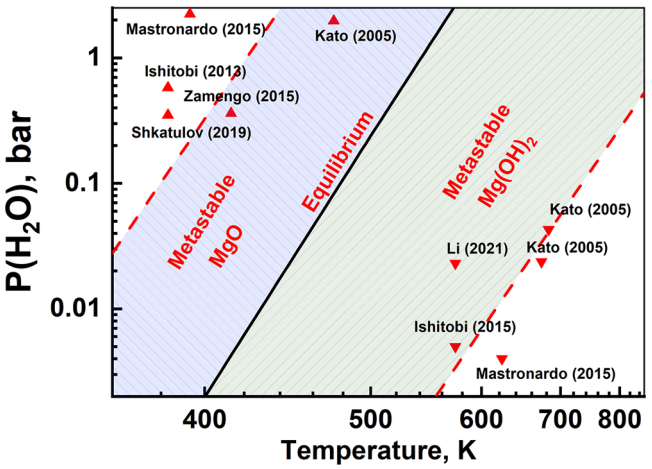

Figure 2. Phase diagram illustrating the equilibrium (black line) and the metastable behavior (red dashed lines) of the $Mg(OH)_2$−MgO transformation based on a literature survey.[11−16]

Such metastable behavior is caused by the high energy barrier of the underlying structural transformations. To boost these processes, ongoing efforts are dedicated to the explorative search for suitable catalysts. Along this line, some inorganic salts (nitrates, chlorides, and acetates of Li, Na, and K) were experimentally shown to be promising for the catalysis of de- and rehydration $Mg(OH)_2$, as well as carbonation of MgO.[11,18−20] Indeed, dramatic differences in the reactivity of MgO with various nitrates still remain to be fully understood.[16,18,21] The fastest progress in understanding is achieved for carbonation of nitrate-doped $MgCO_3$, for which numerous combinations of nitrate dopants were studied,[10,22] a dissolution/crystallization mechanism was established,[23] and the crucial role of the interface was found.[24]

The pronounced liquid/solid interface plays an important role in these systems.[22] It was hypothesized that the reactivity enhancement could be explained quantitatively by accounting for the interfacial energy of molten salt/solid MgO in reaction thermodynamics.[18,25] While the MD simulations for nitrates on MgO were performed,[26] it is yet unclear how the nitrate/MgO interfaces looks like, what are the interface energies, and how they change with composition of the nitrate melt, especially for the most relevant nitrates such as $LiNO_3$, or eutectic mixtures. This knowledge is crucial for the in-depth understanding of the metastability in nitrate/MgO with respect to charging and discharging reactions (Figure 1). The molecular dynamics (MD) modeling could clarify these questions. While the ab initio MD is able to capture subtle features of the interfaces[27] and rearrangement of chemical bonds, its high computational cost and sensibility to the basis[28] make this option less attractive in comparison with traditional MD with experimentally verified interatomic potentials.

In the present work, we use molecular dynamics simulations of nitrate/MgO interfaces for three nitrates ($LiNO_3$, $NaNO_3$, and KNO_3) and the triple nitrate eutectic mixture to provide structural insights into the adsorbed layers, calculate adhesion energies, and relate them to the dehydration/hydration temperature for one of the most promising systems with the smallest metastable zone, namely, $LiNO_3/Mg(OH)_2$.[29,30]

METHODS

Molecular mechanics models were adopted from the literature with a focus on interaction potentials relying on formal charges for the cations, such that the full range of metal ion mixtures may be addressed. The interaction potentials of MgO (Mg−Mg, Mg−O, and O−O) were adopted from the Lewis−Catlow model with formal charges[31] with parameters from ref 32. The model shows good results for the mechanical properties and the melting point in accordance with our simulations. The interaction potential between all three pairs of atoms consists of Coulombic and Buckingham parts (Table 1):

$$U(r_{ij}) = U_C(r_{ij}) + U_{bck}(r_{ij}) \quad (2)$$

$$U_C(r_{ij}) = \sum_i \sum_{j\neq i} \frac{q_i q_j}{\varepsilon r_{ij}} \quad (3)$$

$$U_{bck}(r_{ij}) = \frac{q_i q_j}{r_{ij}} + A_{ij}\exp(-r_{ij}/\rho_{ij}) - \frac{C_{ij}}{r_{ij}^6} \quad (4)$$

Table 1. Buckingham Parameters for Interactions in MgO[32]

interaction	A/eV	ρ/Å	C/(eV Å^6)
Mg^{2+}−O^{2-}	821.6	0.3242	0.0
O^{2-}−O^{2-}	22764.0	0.1490	27.88
Mg^{2+}−Mg^{2+}	0		0

The model for XNO_3/MgO (X = Na, K) was adopted from the works of Anagnostopoulos et al.[26,33] In order to model the whole set of interactions, these authors adopted the model of Jarayaman et al. with formal charges for cations and anions[34] by approximating the Buckingham potentials with Lennard-Jones potentials and using the Lorentz−Berthelot mixing rules (eqs 7 and 8) to define interatomic potentials for interactions between XNO_3 (X = Na, K) and MgO. The Lennard-Jones parameters for Li^+ ions were taken from the work of Rushton[35] to extend the model of Anagnostopoulos. It is noteworthy that the parameter mixing approach was experimentally verified by Anagnostopoulos and resulted in correct contact angle for a $NaNO_3$ droplet on MgO slabs.[26]

Thus, all the interatomic interactions except those in Table 1 were modeled by eqs 5, 3, 6−8, which included mixing rules (Table 2):

$$U(r_{ij}) = U_C(r_{ij}) + U_{LJ}(r_{ij}) \quad (5)$$

$$U_{LJ}(r_{ij}) = 4\varepsilon_{ij}\left[\left(\frac{\sigma_{ij}}{r_{ij}}\right)^{12} - \left(\frac{\sigma_{ij}}{r_{ij}}\right)^{6}\right] \quad (6)$$

$$\varepsilon_{ij} = \sqrt{\varepsilon_i \varepsilon_j} \quad (7)$$

$$\sigma_{ij} = \frac{\sigma_i + \sigma_j}{2} \quad (8)$$

The model for the NO_3^- ions was also adopted from the work of Jayaraman et al.[34] Therein, the N−O bonds are modeled by harmonic potentials (Table 3):

$$U_b = k_b(r - r_0)^2 \quad (9)$$

The O−N−O angular interactions were accounted for by

https://doi.org/10.1021/acsomega.2c00095
ACS Omega 2022, 7, 16371−16379

Table 2. Lennard-Jones Parameters for Interactions X−NO_3 and XNO_3−MgO[26,33,35]

atom	charge	ε/eV	σ/Å
Li	+1	5.0×10^{-9}	6.0707
Na	+1	0.0056373	2.3
K	+1	0.00433641	3.188325
N	+0.95	0.0073719	3.10669
O_{XNO_3}	−0.65	0.006938258	3.00939
Mg	+2	2.253319968	1.501
O_{MgO}	−2	0.005020786	3.369

Table 3. Intramolecular Parameters for Nitrate Ions[34]

interaction		
bond (N−O)	k_b = 525.0 kcal mol^{-1} $Å^{-2}$	r_0 = 1.2676 Å
angle (O−N−O)	k_θ = 105.0 kcal/mol/rad^2	θ_0 = 120.0°
improper (NO_3)	k_ψ = 60.00 kcal/mol/rad^2	ψ_0 = 0.00°

$$U_\theta = k_\theta(\theta - \theta_0)^2 \quad (10)$$

in combination with an improper torsion type function that keeps NO_3 planar:

$$U_\Psi = k_\Psi(\Psi - \Psi_0)^2 \quad (11)$$

Molecular dynamics simulations were carried out by the large-scale atomic/molecular massively parallel simulator (LAMMPS) code.[36] The trajectory of each particle is obtained by integration of Newton's equations of motion with a 1 fs time step. The cutoff distance for the van der Waals and the real-space part of the Coulombic interactions was set to 11 Å, whereas Ewald summation is applied for the long-range contributions. Visual molecular dynamics software (VMD)[37] was used for simple structural analyses and visualization.

The simulation systems were prepared as "sandwich" models, initially consisting of crystalline $NaNO_3$ (8 × 12 × 5 unit cells) on top of a (001) MgO slab (10 × 10 × 10 unit cells). The MgO slab thus was exposed by its (001) surface that is the most relevant for real cubic crystals of MgO. This setup was transformed into a nitrate melt/MgO solid system using several consecutive steps that carefully avoid artificial defect formation (Figure 3).

In step 1, the system was allowed to pre-relax at 1 K (time step, 0.1 fs; *NVT*) to fill the gaps in the nitrate phase due to the lattice mismatch between $NaNO_3$ and MgO. The resulting glassy nitrate phase was then heated up to 3000 K (time step 1 fs) in step 2, using the anisotropic barostat (*NpT*). At this stage, the MgO atoms are kept frozen to enable full melting and spatial relaxation of the nitrate melt without compromising the MgO crystal. After propagating for 5 ns, good decorrelation from the $NaNO_3$ crystal was ensured. The other nitrate phases were prepared from this state by substituting the Na^+ cations with the cation(s) of interest, namely, Li^+ or K^+, or mixed cationic composition with Li^+:Na^+:K^+ = 0.38:0.18:0.44 corresponding to the triple eutectic mixture.[38] After such substitutions, the system was relaxed for another 2 ns at 3000 K.

In step 3, the systems were cooled from 3000 to 773 K in 1 ns. Next, the MgO atoms were unfixed and each simulation was propagated for 10 ns in the *NpT* ensemble (1 atm, 773 K) without geometry restraints (Figure 3). Periodic boundaries were applied for all directions, and p = 1 atm is applied in the anisotropic barostat. It is noteworthy that, on the basis of the autocorrelation functions, the characteristic times of energy decorrelation for these systems did not exceed 0.01 ns which means that nanoseconds-scale simulations provide hundreds of uncorrelated data points (Figure S1 the Supporting Information).

The resulting "sandwich" systems at 773 K, 1 atm conditions consisted of the (001) MgO slab of 42 × 42 × 42 $Å^3$ and an approximately similar volume of a nitrate melt. Due to the extended ordering in the case of KNO_3 the amount of liquid phase was doubled before step 3 to ensure the presence of several nanometers scale bulk liquid in the system.

In order to calculate the adhesion energy, the nitrate/MgO interfaces were compared to isolated phases of MgO and nitrate with and without surface. The relaxed bulk nitrate melts without MgO were sampled from 5 ns simulations in an *NpT* ensemble at 1 atm and 773 K. Separately, similar systems with flat surfaces were sampled from *NVT* simulations at 773 K. The same procedure was performed for MgO without nitrate.

All of the energy averages were assessed from Gaussian fits of the corresponding occurrence profiles. The statistical data are provided in the Supporting Information.

RESULTS AND DISCUSSION

Structure of Adsorbed Layers. While cooling from 3000 to 773 K (step 3 in Figure 3), a static monolayer of adsorbed nitrate is formed on the surface of MgO. The layer contains both nitrate ions and corresponding cations adsorbed in an ordered manner as shown for $LiNO_3$/MgO and (Li,Na,K)-NO_3/MgO in Figure 4 and for $NaNO_3$ and KNO_3 in the Supporting Information (Figure S2).

The cations (Li^+, Na^+, and K^+) are attracted to the oxygen atoms with average distances d(X) in the range of 2.17−2.84

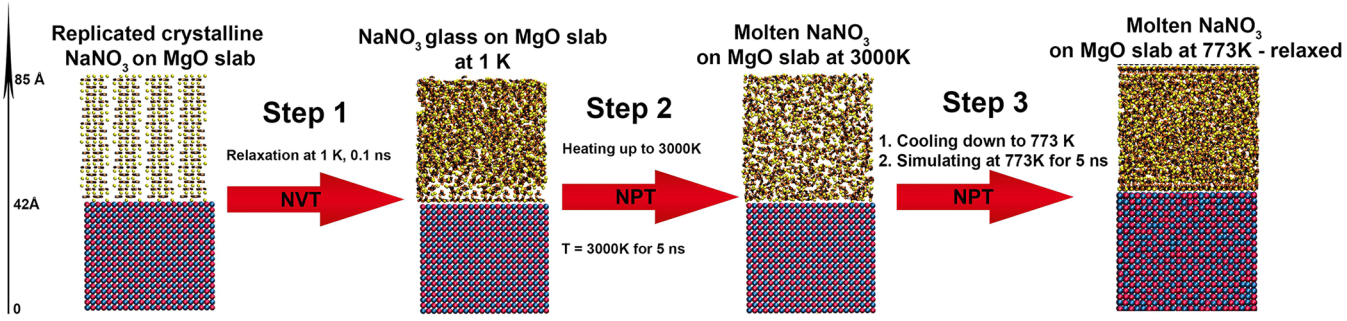

Figure 3. Scheme of simulations for $NaNO_3$/MgO. Other cationic compositions were obtained by substituting Na^+ before the third step at 3000 K, followed by additional XNO_3 relaxation for 2 ns.

https://doi.org/10.1021/acsomega.2c00095
ACS Omega 2022, 7, 16371−16379

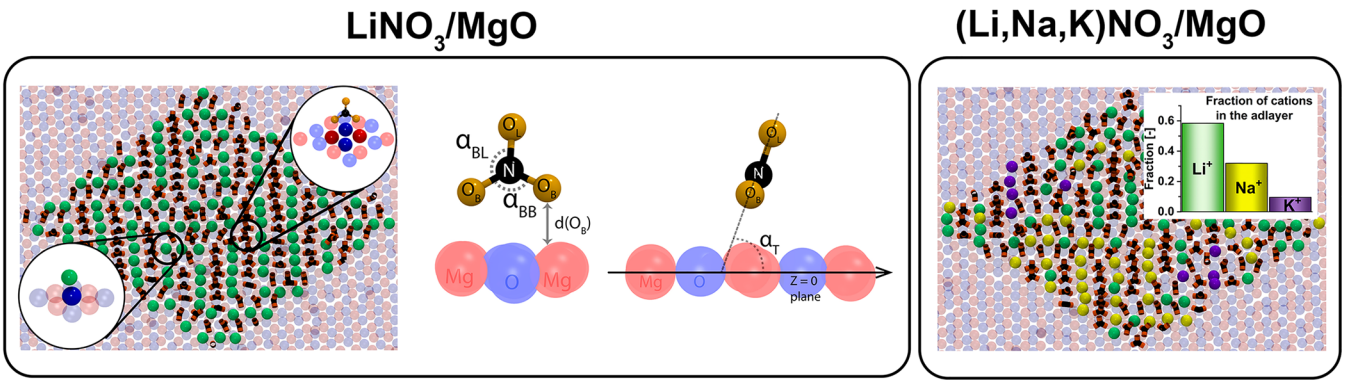

Figure 4. Structure of adsorbed monolayers of $LiNO_3$ (left) and triple eutectic mixture $(Li,Na,K)NO_3$ (right) on a (001) MgO slab. Both systems are shown from a tilted view direction to illustrate ordering of the adlayers. The picture on the left also illustrates primary adsorption centers for Li^+ cation and coordination of nitrate ion to MgO layer as well as main geometric parameters of the nitrate; the distances and the angles are calculated on the basis of coordinates of atomic centers. The inset on the right figure shows the fraction of each cation type in the first adlayer. Colors: Mg, red; O(MgO), blue; Li, green; Na, yellow; K, violet; O(NO), orange; N, black.

Table 4. Average Geometric Parameters for the Adlayer of XNO_3 on a MgO Slab[a]

system	d(X), Å	d(N), Å	$d(O_B)$, Å	α_{BB}, deg	α_{BL}, deg	α_T, deg
$LiNO_3$/MgO	2.17	3.17	2.38	119.68	120.16	86.49
$NaNO_3$/MgO	2.28	3.34	2.5	119.30	120.35	89.85
KNO_3/MgO	2.84	3.08	2.5	119.50	120.25	87.72
$(Li,Na,K)NO_3$/MgO	2.30	3.18	2.42	119.10	120.45	87.46

[a]Distribution and standard deviations can be found in the Supporting Information (Figures S3 and S4). d(X), average shortest distance between cations in adlayer and MgO slab; d(N), average shortest distance between nitrogen in adlayer and MgO slab; $d(O_B)$, average shortest distance between oxygens O_B (Figure 4) in adlayer and MgO slab; α_{BB}, average angle O_B-N-O_B in the adlayer; α_{BL}, average angle O_B-N-O_L in the adlayer; α_T, tilt angle between nitrate plane and the MgO slab.

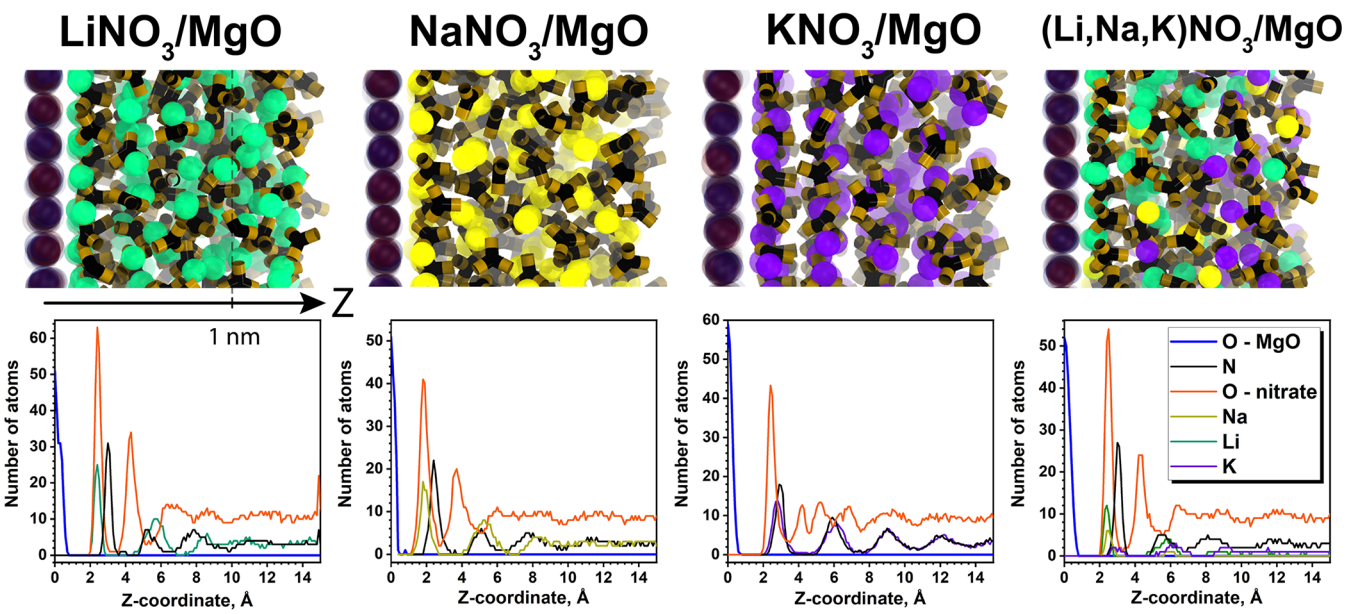

Figure 5. Adsorbed layers and distribution of atoms in them across Z-axis (normal to MgO surface). Colors: Li, green; Na, yellow; K, violet; Mg, red; O(MgO), black; N, orange; $O(NO_3)$, orange.

Å, increasing with the cationic radius in the row $Li^+-Na^+-K^+$ (Table 4). For Li^+ the distance almost perfectly matches the Mg−O distance in the MgO crystal due to very close cationic radii.[39] This is in line with the finding that for the mixed nitrate $(Li,Na,K)NO_3$/MgO interface the predominant cation at the contact layer is Li^+, thus suggesting higher adsorption energy due to better geometric fitting.

The oxygen atoms from the nitrate are coordinated to pairs of Mg^{2+} ions adjacent to each other in diagonal direction [110] in the plane (Figure 3, left inset). The average tilt angle, α_T, between the plane of nitrate (O_B-N-O_B) and the MgO (001) plane is close to 90°, suggesting almost perpendicular orientation of nitrate with respect to the MgO surface. However, the high standard deviation of α_T of about 45°

https://doi.org/10.1021/acsomega.2c00095
ACS Omega 2022, 7, 16371−16379

(Figure S3) suggests high thermal mobility of adsorbed nitrate with respect to tilting.

For the adsorbed nitrate ions, the distances between nitrogen and surface-bound oxygens from nitrate (N−O_B) are equal to the distances between nitrogen and loose oxygen atoms of nitrate (N−O_L) for all of the studied systems (1.26 Å, Figure S3). The angles O_B−N−O_B (α_{BB}) and O_B−N−O_L (α_{BL}) are also mutually equal: $\alpha_{BB} \approx \alpha_{BL} \approx 120°$ (standard deviation ∼ 5°). Thus, the nitrate geometry is not distorted by adsorption.

The distance between bound oxygen atoms O_B of nitrates (Figure 4, left inset) and the closest MgO atoms slightly increases in the row $LiNO_3$−$NaNO_3$−KNO_3, with the $LiNO_3$ system exhibiting the closest one to the Mg−O distance in MgO (2.1 Å). Thus, the adsorbed monolayer exhibits geometric parameters that tend to match the ordered structural motifs of MgO, and the best fit is observed for adsorbed the monolayer of $LiNO_3$.

The interface ordering is not limited to the monolayer. The Z-distribution profiles (Figure 5) suggest that at least two layers after the first one are partially ordered as there are at least two more peaks of cations and nitrogen before the distribution curve becomes flat corresponding to average numbers of distribution in bulk liquid nitrate at z = 10−12 Å. In the case of KNO_3/MgO three additional peaks are observed instead of two, and the ordering is observed up to 15 Å. A possible reason for this is the dominant contribution of Coulombic interactions in the chosen potentials that favor packing of ions. The increase of ionic radii in the row Li−Na−K and its approach to the anion radius make such packing more favorable, which is expressed in the deeper "ordering" for KNO_3.

Thus, the interface consists of several (3−4) ordered layers of nitrate with the first ordered layer (adlayer) geometrically matching the structure of MgO. The match is the closest for the case of $LiNO_3$, which could be the reason of predominance of Li^+ cations in the adlayer for the system with triple eutectics (Li,Na,K)NO_3.

Adhesion and Dispersion Energy. Adhesion energy, E_a, by definition[40] is the work required to divide the interface (nitrate/MgO) into the two constituents, thus creating two surfaces (MgO and nitrate):

$$E_a = E_{MgO/vac} + E_{XNO_3/vac} - E_{XNO_3/MgO} \quad (12)$$

We furthermore define the "intercalation" energy, E_i, that reflects the insertion of the MgO slab into bulk nitrate melts:

$$E_i = E_{MgO/vac} + E_{XNO_3} - E_{XNO_3/MgO} \quad (13)$$

In addition, the surface energy for MgO and individual nitrate melts were defined as

$$E_s(MgO) = E_{MgO/vac} - E_{MgO} \quad (14)$$

$$E_s(XNO_3) = E_{XNO_3/vac} - E_{XNO_3} \quad (15)$$

For such set of definitions, it is fulfilled that

$$E_a = E_s + E_i \quad (16)$$

The two contributions to E_a can be derived from the conducted set of simulations (Figure 6).

The surface energy E_s for MgO per unit surface is 1.15 J/m^2, which is in excellent agreement with the literature experimental data.[41,42]

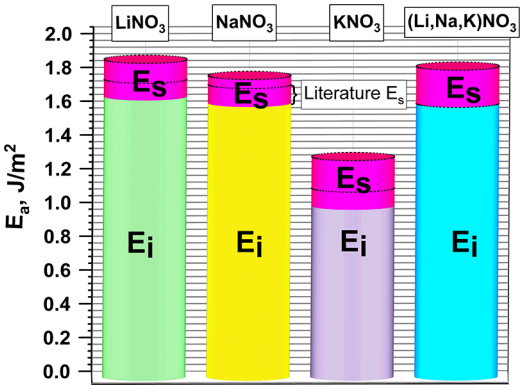

Figure 6. Interfacial (E_i), surface (E_s), and adhesion (E_a) energies for XNO_3/MgO (X = Li, Na, K, and Li + Na + K) systems.

The surface energies, E_s, of nitrates (magenta part of Figure 6) are overestimated by 0.05−0.1 J/m^2 (indicated by the dashed line) in comparison with experimental values from the literature.[43] The origin of this overestimation is likely a systematic error of the interaction potential for the nitrates approximated by Lennard-Jones functions.

Both E_a and E_i values for all of the systems exceed the MgO surface energy which suggests that formation of interfaces is thermodynamically favorable in nitrate/MgO systems, as was experimentally evidenced for other ionic oxides.[44]

Finally, the self-dispersion energy E_{disp} can be defined as energy required to form bulk nitrate and bulk MgO from the "sandwich" system:

$$E_{disp}(XNO_3) = E_{XNO_3} + E_{MgO} - E_{XNO_3/MgO} \quad (17)$$

The calculation by using Hess law (Figure 7) for $LiNO_3$/MgO yields 0.53 J/(1 m^2 of the interface). Similar calculation yields lower values for other nitrates (inset in Figure 7) with KNO_3 being almost zero. Thus, for the case of KNO_3, the weakest interaction with the surface is observed and it is not clear from the present calculation whether the dispersion of KNO_3 is thermodynamically favorable.

Role of Interface in Metastability of $Mg(OH)_2$. The data concerning interface energetics could be useful for understanding the effect of salt dopants on the metastability of process 1 reported in numerous works.[13,16,17,45,46] One of them[47] reports a decrease of dehydration temperature for $LiNO_3$ (5 wt %)/$Mg(OH)_2$ in comparison with pure $Mg(OH)_2$, which was accompanied by dramatic reduction of the specific surface area of the product from 250 m^2/g for pure MgO to 21 m^2/g for $LiNO_3$/MgO. This effect may be quantified thermodynamically if one considers the contribution of surfaces and interfaces to the thermodynamics of process 1, namely, to free formation energy of reagents and products.

To illustrate this approach, we consider the equilibrium of bulk solid phases:

$$Mg(OH)_{2(bulk)} \rightleftharpoons MgO_{(bulk)} + H_2O(g) \quad (18)$$

and compare it to the metastable pseudoequilibrium state with highly disperse MgO originating from bulk $Mg(OH)_2$:

$$Mg(OH)_{2(bulk)} \rightleftharpoons MgO_{(disp)} + H_2O(g) \quad (19)$$

It was experimentally found that due to the metastability, the real dissociation pressure over $Mg(OH)_2$ is less than calculated from thermodynamic parameters of the bulk phases for

https://doi.org/10.1021/acsomega.2c00095
ACS Omega 2022, 7, 16371−16379

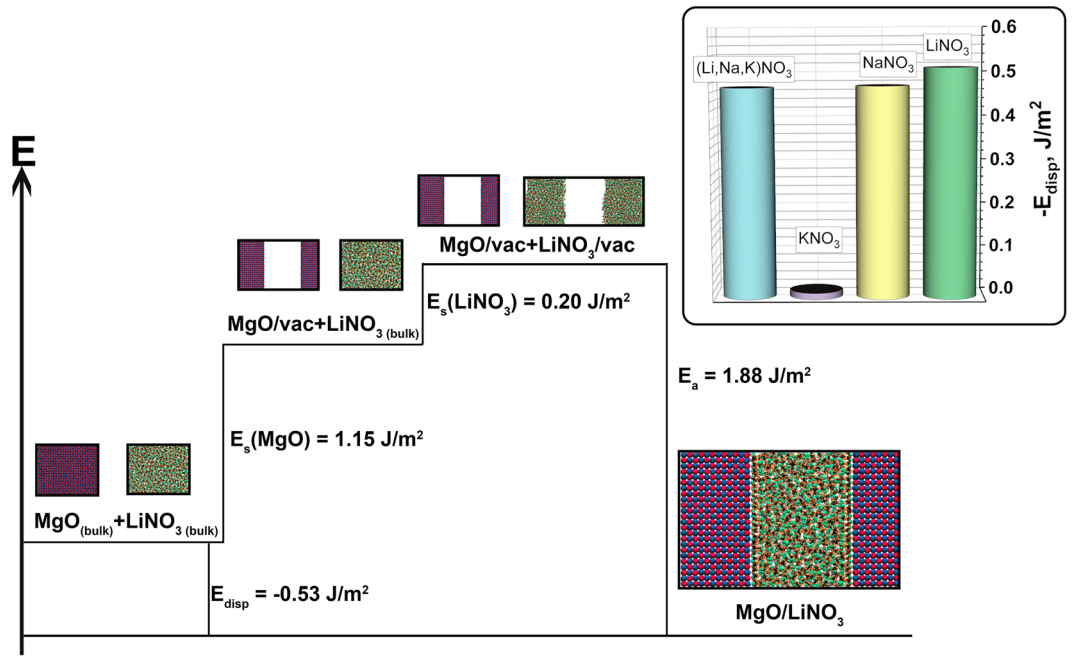

Figure 7. Calculation of dispersion energy E_{disp} for the $LiNO_3$/MgO system.

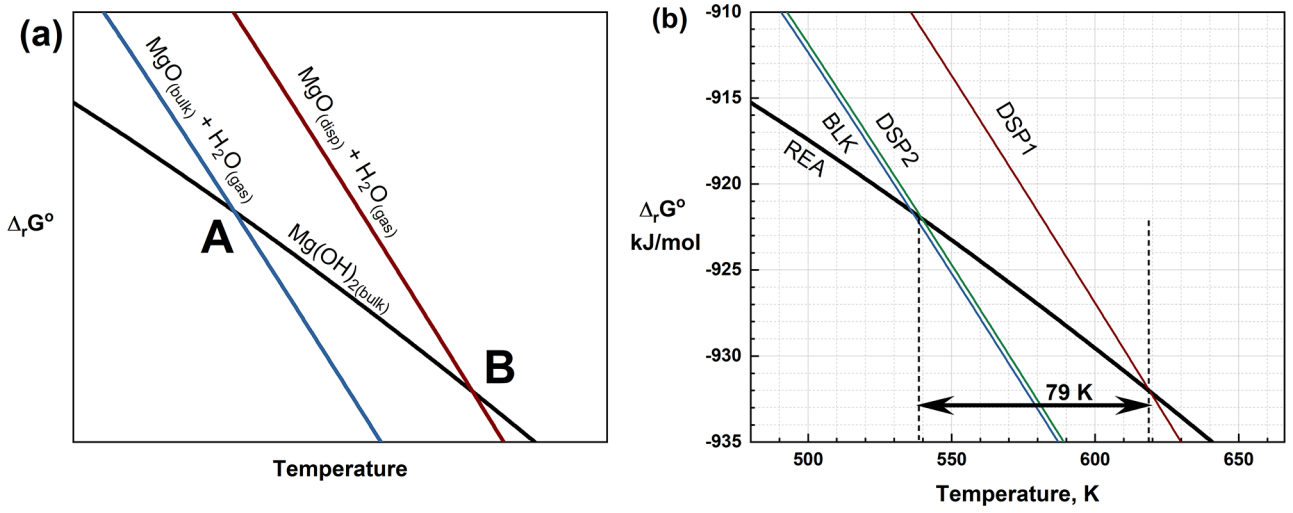

Figure 8. Diagram $\Delta_f G^\circ - T$ illustrating bulk and metastable equilibria for dehydration of pure $Mg(OH)_2$ (a) and $LiNO_3/Mg(OH)_2$ (b). REA, reagents; BLK, bulk products; DSP1, disperse products without interaction with the $LiNO_3$ additive; DSP2, represents disperse products with interaction with $LiNO_3$ additive.

equilibrium 18.[48] In other words, equilibrium 19 is observed under milder decomposition conditions (T = 300−350 °C), while equilibrium 18 is attainable only at high temperature and pressures (T > 500 °C; P ∼ 10 bar), allowing for sintering of the product particles.[49]

The difference between the two equilibria may be attributed to extra surface energy increasing the free formation energy of MgO, thus increasing $\Delta_r G(T)$ for reaction 19 in comparison with reaction 18. It can be better illustrated in terms of the following formalism. Equilibrium 18 is defined by the equation of free formation energies of reagents (hydroxide) and products (oxide + vapor):

$$\Delta_f G^\circ(\mathrm{Mg(OH)_2(bulk)}) = \Delta_f G^\circ(\mathrm{MgO}) + \Delta_f G^\circ(\mathrm{H_2O}) \quad (20)$$

The intersection of left and right parts of equation 20 as functions of temperature corresponds to the equilibrium of bulk phases of $Mg(OH)_2$ and MgO (intersection point A in Figure 8a). For the case of disperse MgO, the surface energy term $\Delta_{surf}G^\circ(MgO)$ is added to the right part, thus shifting the intersection point to higher temperatures (point B in Figure 8a):

$$\Delta_f G^\circ(\mathrm{Mg(OH)_2(bulk)}) = \Delta_f G^\circ(\mathrm{MgO}) + \Delta_f G^\circ(\mathrm{H_2O}) + \Delta_{surf} G^\circ(\mathrm{MgO}) \quad (21)$$

This shift to higher temperature may be interpreted as metastability with respect to equilibrium 18. The surface energy $\Delta_{surf}G^\circ(MgO)$ may be approximated by specific surface

https://doi.org/10.1021/acsomega.2c00095
ACS Omega 2022, 7, 16371−16379

energy multiplied by surface of MgO under consideration (e.g., 250 m^2/g):

$$\Delta_{surf} G^{O}(MgO) \approx E_s S \quad (22)$$

This formalism is applied here to calculate the temperature difference for dehydration of pure $Mg(OH)_2$ and modified with $LiNO_3$. For the latter case the following processes are considered:

$$LiNO_{3(bulk)} + Mg(OH)_{2(bulk)} \rightleftharpoons LiNO_3/MgO_{(disp)} + H_2O(g) \quad (23)$$

$$LiNO_{3(bulk)} + Mg(OH)_{2(bulk)} \rightleftharpoons LiNO_{3(bulk)} + MgO_{(bulk)} + H_2O(g) \quad (24)$$

$$LiNO_{3(bulk)} + Mg(OH)_{2(bulk)} \rightleftharpoons LiNO_{3(bulk)} + MgO_{(disp)} + H_2O(g) \quad (25)$$

We will consider the following states on the $\Delta_f G^\circ - T$ diagram (Figure 7b):

- REA: reagents of processes 23−25, i.e., non-interacting bulk $Mg(OH)_2$ and bulk $LiNO_3$
- BLK: products of process 24, i.e., non-interacting bulk MgO and bulk $LiNO_3$
- DSP1: products of process 25, i.e., non-interacting disperse MgO (S_1 = 250 m^2/g) and bulk $LiNO_3$
- DSP2: products of process 23, i.e., disperse $LiNO_3$/MgO (S_2 = 25 m^2/g) with pronounced interface between $LiNO_3$ and MgO

The observed temperature difference between dehydration temperatures of pure and $LiNO_3$-doped $Mg(OH)_2$ may be evaluated in this concept as the equilibrium temperature difference between the equilibria REA−DSP2 and REA−DSP1. Both equilibria may be determined from the thermodynamic data for the bulk phases from the literature[50] and specific surface or interface energies as follows:

$$\Delta_f G^\circ(DSP1) \approx \Delta_f G^\circ(BLK) + E_s(MgO) S_1 \quad (26)$$

for DSP1 state and

$$\Delta_f G^\circ(DSP2) \approx \Delta_f G^\circ(BLK) + E_{disp} S_2 \quad (27)$$

for DSP2 state. Both E_s and E_{disp} were determined by relaxation of the MgO surface or the $LiNO_3$/MgO interface as described above.

Such calculation gives the temperature difference, ΔT, between dehydration temperatures of $Mg(OH)_2$ and $LiNO_3$/$Mg(OH)_2$ (5 wt % $LiNO_3$) of 79 K. This temperature difference is in good agreement with 76 K as found in ref 18 and confirmed later in ref 16. The difference between REA−BLK and REA−DSP2 is only 4.5 K, which suggests that the state DSP2 is thermodynamically very close to the bulk state BLK. Thus, the catalyst almost completely brings the system to the equilibrium of bulk phases.

CONCLUSIONS

In this work, we present molecular dynamics simulations of nitrate/MgO sandwich models to characterize the structure of the interfaces, calculate interfacial energies, and discuss how this knowledge helps in understanding the catalysis of $Mg(OH)_2$ dehydration.

The modeling based on experimentally verified potentials allowed highlighting the structural features of the interface. The nitrates form ordered layers (extended over 9−12 Å) next to the MgO surface. Oxygen atoms are the primary adsorption centers for cations, while nitrates are adsorbed to Mg via two coordinating oxygen atoms, the angle between the nitrate plane and the MgO slab is close to 90°. For the triple eutectic mixture Li ions prevail in the adlayer, followed by Na and K ions.

The adsorption of nitrate leads to high adhesion energy, E_a, ranging from 1.3 J/m for KNO_3 to 1.8 J/m for $NaNO_3$ to 1.9 J/m^2 for $LiNO_3$, which makes creation of such interfaces thermodynamically favorable.

The calculated values help in understanding the difference of equilibrium temperatures for the dehydration of $LiNO_3$/$Mg(OH)_2$ and $Mg(OH)_2$. The developed formalism consists of analysis of thermodynamic data for bulk and dispersed products, using the values of adhesion and dispersion energies from the MD modeling. Our theoretical estimate for this system (79 K) on the basis of the thermodynamic formalism is close to the experimental value (76 K).

In general, the data on specific surfaces of the resultant oxides in combination with knowledge of interfacial energies reported here may be used to thermodynamically quantify how far is a thermochemical system from the bulk equilibrium, thus predicting the potential effect for new nitrate-based dopants.[16] Thus, it may be possible to put this approach in a broader context and apply it to other systems involving MgO and catalytic additives, for instance, $NaNO_3$/hydromagnesite[21] or nitrate mixtures/$MgCO_3$.[22]

ASSOCIATED CONTENT

Supporting Information

The Supporting Information is available free of charge at https://pubs.acs.org/doi/10.1021/acsomega.2c00095.

Energy autocorrelation functions of ion pair interaction energies at 773 K; appearance of the first adsorbed layer for $NaNO_3$/MgO and KNO_3/MgO; distribution of shortest distances between the MgO surface and atoms of the adlayer; distribution of distances and angles in the adlayer; total energy distribution at 773 K (PDF)

AUTHOR INFORMATION

Corresponding Author

Alexandr Shkatulov − *Department of Applied Physics, Eindhoven University of Technology, Eindhoven 5612 AP, The Netherlands*; orcid.org/0000-0002-9765-104X; Email: a.shkatulov@tue.nl

Authors

Bahanur Becit − *Computer Chemistry Centre (CCC), Friedrich-Alexander-Universität Erlangen-Nürnberg, Erlangen 91052, Germany*

Dirk Zahn − *Computer Chemistry Centre (CCC), Friedrich-Alexander-Universität Erlangen-Nürnberg, Erlangen 91052, Germany*

Complete contact information is available at: https://pubs.acs.org/10.1021/acsomega.2c00095

https://doi.org/10.1021/acsomega.2c00095
ACS Omega 2022, 7, 16371−16379

Notes

The authors declare no competing financial interest.

■ ACKNOWLEDGMENTS

The work has been performed under Project HPC-EUROPA3 (INFRAIA-2016-1-730897), with the support of the EC Research Innovation Action under the H2020 Programme; in particular, we gratefully acknowledge the support of the Computer Chemistry Centre at Friedrich-Alexander-Universität Erlangen-Nürnberg and the computer resources and technical support provided by High Performance Computing Center HLRS (Dr. A. Cheptsov and O. Rudyy).

■ REFERENCES

(1) *World Energy Outlook 2020*, International Energy Agency (IEA), Paris, 2020; https://www.iea.org/reports/world-energy-outlook-2020 (accessed 2021-03-28).
(2) Carrillo, A. J.; González-Aguilar, J.; Romero, M.; Coronado, J. M. Solar Energy on Demand: A Review on High Temperature Thermochemical Heat Storage Systems and Materials. *Chem. Rev.* **2019**, *119*, 4777−4816.
(3) Firth, A.; Zhang, B.; Yang, A. Quantification of Global Waste Heat and Its Environmental Effects. *Appl. Energy* **2019**, *235*, 1314−1334.
(4) Manz, P.; Kermeli, K.; Persson, U.; Neuwirth, M.; Fleiter, T.; Crijns-Graus, W. Decarbonizing District Heating in EU-27 + UK: How Much Excess Heat Is Available from Industrial Sites? *Sustainability Switz.* **2021**, *13* (3), 1439.
(5) Bianchi, G.; Panayiotou, G. P.; Aresti, L.; Kalogirou, S. A.; Florides, G. A.; Tsamos, K.; Tassou, S. A.; Christodoulides, P. Estimating the Waste Heat Recovery in the European Union Industry. *Energy Ecol. Environ.* **2019**, *4* (5), 211−221.
(6) Borri, E.; Zsembinszki, G.; Cabeza, L. F. Recent Developments of Thermal Energy Storage Applications in the Built Environment: A Bibliometric Analysis and Systematic Review. *Appl. Therm. Eng.* **2021**, *189*, 116666.
(7) Calderón, A.; Barreneche, C.; Hernández-Valle, K.; Galindo, E.; Segarra, M.; Fernández, A. I. Where Is Thermal Energy Storage (TES) Research Going? − A Bibliometric Analysis. *Sol. Energy* **2020**, *200*, 37−39.
(8) Stengler, J.; Linder, M. Thermal Energy Storage Combined with a Temperature Boost: An Underestimated Feature of Thermochemical Systems. *Appl. Energy* **2020**, *262*, 114530.
(9) Desai, F.; Sunku Prasad, J.; Muthukumar, P.; Rahman, M. M. Thermochemical Energy Storage System for Cooling and Process Heating Applications: A Review. *Energy Convers. Manag.* **2021**, *229*, 113617.
(10) Shkatulov, A. I.; Kim, S. T.; Miura, H.; Kato, Y.; Aristov, Yu. I. Adapting the MgO-CO2 Working Pair for Thermochemical Energy Storage by Doping with Salts. *Energy Convers. Manage.* **2019**, *185*, 473−481.
(11) Shkatulov, A.; Takasu, H.; Kato, Y.; Aristov, Y. Thermochemical Energy Storage by LiNO3-Doped Mg(OH)2: Rehydration Study. *J. Energy Storage* **2019**, *22*, 302−310.
(12) Mastronardo, E.; Bonaccorsi, L.; Kato, Y.; Piperopoulos, E.; Milone, C. Efficiency Improvement of Heat Storage Materials for MgO/H2O/Mg(OH)2 Chemical Heat Pumps. *Appl. Energy* **2016**, *162*, 31−39.
(13) Ishitobi, H.; Uruma, K.; Takeuchi, M.; Ryu, J.; Kato, Y. Dehydration and Hydration Behavior of Metal-Salt-Modified Materials for Chemical Heat Pumps. *Appl. Therm. Eng.* **2013**, *50* (2), 1639−1644.
(14) Kato, Y.; Sasaki, Y.; Yoshizawa, Y. Magnesium Oxide/Water Chemical Heat Pump to Enhance Energy Utilization of a Cogeneration System. *Energy* **2005**, *30* (11−12), 2144−2155.
(15) Zamengo, M.; Ryu, J.; Kato, Y. Chemical Heat Storage of Thermal Energy from a Nuclear Reactor by Using a Magnesium Hydroxide/Expanded Graphite Composite Material. *Energy Procedia* **2015**, *71*, 293−305.
(16) Li, M.-T.; Li, Y.-T.; Sun, L.; Xu, Z.-B.; Zhao, Y.; Meng, Z.-H.; Wu, Q.-P. Tremendous Enhancement of Heat Storage Efficiency for Mg(OH)2-MgO-H2O Thermochemical System with Addition of Ce(NO3)3 and LiOH. *Nano Energy* **2021**, *81*, 105603.
(17) Shkatulov, A. I.; Aristov, Y. Thermochemical Energy Storage Using $LiNO_3$-Doped $Mg(OH)_2$: A Dehydration Study. *Energy Technol.* **2018**, *6* (9), 1844−1851.
(18) Shkatulov, A.; Krieger, T.; Zaikovskii, V.; Chesalov, Y.; Aristov, Y. Doping Magnesium Hydroxide with Sodium Nitrate: A New Approach to Tune the Dehydration Reactivity of Heat-Storage Materials. *ACS Appl. Mater. Interfaces* **2014**, *6* (22), 19966−19977.
(19) Kurosawa, R.; Takeuchi, M.; Ryu, J. Fourier-Transform Infrared Analysis of the Dehydration Mechanism of $Mg(OH)_2$ and Chemically Modified $Mg(OH)_2$. *J. Phys. Chem. C* **2021**, *125* (10), 5559−5571.
(20) Dal Pozzo, A.; Armutlulu, A.; Rekhtina, M.; Abdala, P. M.; Müller, C. R. CO2 Uptake and Cyclic Stability of MgO-Based CO2 Sorbents Promoted with Alkali Metal Nitrates and Their Eutectic Mixtures. *ACS Appl. Energy Mater.* **2019**, *2* (2), 1295−1307.
(21) Rekhtina, M.; Dal Pozzo, A.; Stoian, D.; Armutlulu, A.; Donat, F.; Blanco, M. V.; Wang, Z.-J.; Willinger, M.-G.; Fedorov, A.; Abdala, P. M.; Müller, C. R. Effect of Molten Sodium Nitrate on the Decomposition Pathways of Hydrated Magnesium Hydroxycarbonate to Magnesium Oxide Probed by in Situ Total Scattering. *Nanoscale* **2020**, *12* (31), 16462−16473.
(22) Hu, Y.; Guo, Y.; Sun, J.; Li, H.; Liu, W. Progress in MgO Sorbents for Cyclic CO2 Capture: A Comprehensive Review. *J. Mater. Chem. A* **2019**, *7* (35), 20103−20120.
(23) Bork, A. H.; Rekhtina, M.; Willinger, E.; Castro-Fernández, P.; Drnec, J.; Abdala, P. M.; Müller, C. R. Peering into Buried Interfaces with X-Rays and Electrons to Unveil MgCO3 Formation during CO2 Capture in Molten Salt-Promoted MgO. *Proc. Natl. Acad. Sci. U. S. A.* **2021**, *118* (26), e2103971118.
(24) Gao, W.; Xiao, J.; Wang, Q.; Li, S.; Vasiliades, M. A.; Huang, L.; Gao, Y.; Jiang, Q.; Niu, Y.; Zhang, B.; Liu, Y.; He, H.; Efstathiou, A. M. Unravelling the Mechanism of Intermediate-Temperature CO2 Interaction with Molten-NaNO3-Salt-Promoted MgO. *Adv. Mater.* **2022**, *34* (4), 2106677.
(25) Shkatulov, A.; Aristov, Y. Calcium Hydroxide Doped by KNO_3 as a Promising Candidate for Thermochemical Storage of Solar Heat. *RSC Adv.* **2017**, *7* (68), 42929−42939.
(26) Anagnostopoulos, A.; Navarro, H.; Alexiadis, A.; Ding, Y. Wettability of NaNO3 and KNO3 on MgO and Carbon Surfaces—Understanding the Substrate and the Length Scale Effects. *J. Phys. Chem. C* **2020**, *124* (15), 8140−8152.
(27) Zhou, X.; Zhang, L.; Jiang, B. Hot-Atom-Mediated Dynamical Displacement of CO Adsorbed on Cu(111) by Incident H Atoms: An Ab Initio Molecular Dynamics Study. *J. Phys. Chem. C* **2018**, *122* (27), 15485−15493.
(28) Yamijala, S. S. R. K. C.; Ali, Z. A.; Wong, B. M. Acceleration vs Accuracy: Influence of Basis Set Quality on the Mechanism and Dynamics Predicted by Ab Initio Molecular Dynamics. *J. Phys. Chem. C* **2019**, *123* (41), 25113−25120.
(29) Shkatulov, A.; Aristov, Y. Modification of Magnesium and Calcium Hydroxides with Salts: An Efficient Way to Advanced Materials for Storage of Middle-Temperature Heat. *Energy* **2015**, *85*, 667−676.
(30) Li, S.; Liu, J.; Tan, T.; Nie, J.; Zhang, H. Optimization of LiNO3−Mg(OH)2 Composites as Thermo-Chemical Energy Storage Materials. *J. Environ. Manage.* **2020**, *262*, 110258.
(31) Lewis, G. V.; Catlow, C. R. A. Potential Models for Ionic Oxides. *J. Phys. C Solid State Phys.* **1985**, *18* (6), 1149−1161.
(32) Henkelman, G.; Uberuaga, B. P.; Harris, D. J.; Harding, J. H.; Allan, N. L. MgO Addimer Diffusion on MgO(100): A Comparison of *Ab Initio* and Empirical Models. *Phys. Rev. B* **2005**, *72* (11), 115437.

https://doi.org/10.1021/acsomega.2c00095
ACS Omega 2022, 7, 16371−16379

(33) Anagnostopoulos, A.; Alexiadis, A.; Ding, Y. Molecular Dynamics Simulation of Solar Salt (NaNO3-KNO3) Mixtures. *Sol. Energy Mater. Sol. Cells* **2019**, *200*, 109897.
(34) Jayaraman, S.; Thompson, A. P.; von Lilienfeld, O. A.; Maginn, E. J. Molecular Simulation of the Thermal and Transport Properties of Three Alkali Nitrate Salts. *Ind. Eng. Chem. Res.* **2010**, *49* (2), 559−571.
(35) Rushton, M. J. D.; Grimes, R. W.; Owens, S. L. Partial Ordering of Glass Networks Adjacent to Simulated Glass−Crystal Interfaces. *J. Non-Cryst. Solids* **2011**, *357* (16), 3278−3287.
(36) Thompson, A. P.; Aktulga, H. M.; Berger, R.; Bolintineanu, D. S.; Brown, W. M.; Crozier, P. S.; In 't Veld, P. J.; Kohlmeyer, A.; Moore, S. G.; Nguyen, T. D.; Shan, R.; Stevens, M. J.; Tranchida, J.; Trott, C.; Plimpton, S. J. LAMMPS - a Flexible Simulation Tool for Particle-Based Materials Modeling at the Atomic, Meso, and Continuum Scales. *Comput. Phys. Commun.* **2022**, *271*, 108171.
(37) Humphrey, W.; Dalke, A.; Schulten, K. VMD: Visual Molecular Dynamics. *J. Mol. Graph.* **1996**, *14* (1), 33−38.
(38) Bradshaw, R. W.; Meeker, D. E. High-Temperature Stability of Ternary Nitrate Molten Salts for Solar Thermal Energy Systems. *Sol. Energy Mater.* **1990**, *21* (1), 51−60.
(39) Shannon, R. D. Revised Effective Ionic Radii and Systematic Studies of Interatomic Distances in Halides and Chalcogenides. *Acta Crystallogr., Sect. A* **1976**, *32* (5), 751−767.
(40) Adamson, A. W.; Gast, A. P. *Physical Chemistry of Surfaces*, 6th ed.; Wiley, 1997.
(41) Jura, G.; Garland, C. W. The Experimental Determination of the Surface Tension of Magnesium Oxide. *J. Am. Chem. Soc.* **1952**, *74* (23), 6033−6034.
(42) Hayun, S.; Tran, T.; Ushakov, S. V.; Thron, A. M.; van Benthem, K.; Navrotsky, A.; Castro, R. H. R. Experimental Methodologies for Assessing the Surface Energy of Highly Hygroscopic Materials: The Case of Nanocrystalline Magnesia. *J. Phys. Chem. C* **2011**, *115* (48), 23929−23935.
(43) Janz, G. J.; Krebs, U.; Siegenthaler, H. F.; Tomkins, R. P. T. Molten Salts: Volume 3 Nitrates, Nitrites, and Mixtures: Electrical Conductance, Density, Viscosity, and Surface Tension Data. *J. Phys. Chem. Ref. Data* **1972**, *1* (3), 581−746.
(44) Uvarov, N. F.; Hairetdinov, E.; Skobelev, I. Composite Solid Electrolytes MeNO3-Al2O3 (Me = Li, Na, K). *Solid State Ionics* **1996**, *86−88*, 577−580.
(45) Myagmarjav, O.; Ryu, J.; Kato, Y. Dehydration Kinetic Study of a Chemical Heat Storage Material with Lithium Bromide for a Magnesium Oxide/Water Chemical Heat Pump. *Prog. Nucl. Energy* **2015**, *82*, 153−158.
(46) Sun, L.; Wu, Q.; Zhang, L.; Li, Y.; Li, M.; Gao, T.; Guo, S.; Wang, D. Doping Magnesium Hydroxide with Ce(NO3)3: A Promising Candidate Thermochemical Energy Storage Materials. *IOP Conf. Ser. Earth Environ. Sci.* **2019**, *295*, 032068.
(47) Shkatulov, A. I.; Aristov, Y. Thermochemical Energy Storage Using LiNO3-Doped Mg(OH)2: A Dehydration Study. *Energy Technol.* **2018**, *6* (9), 1844−1851.
(48) Giauque, W. F. An Example of the Difficulty in Obtaining Equilibrium Corresponding to a Macrocrystalline Non-Volatile Phase. The Reaction Mg(OH)2 = MgO + H2O. *J. Am. Chem. Soc.* **1949**, *71*, 3192−3194.
(49) Roy, D. M.; Roy, R. A Re-Determination of Equilibrium in the System MgO-H2O and Comments on Earlier Work. *Am. J. Sci.* **1957**, *255*, 573−582.
(50) Barin, I. *Thermochemical Data of Pure Substances*, 3rd ed.; VCH: Weinheim, Germany, 1997. DOI: 10.1002/9783527619825.

https://doi.org/10.1021/acsomega.2c00095
ACS Omega 2022, 7, 16371−16379